

Transcritical rotating flow over topography

By **J. G. ESLER, O. J. RUMP,**
AND **E. R. JOHNSON**

Department of Mathematics, University College London,
25 Gower Street, London WC1E 6BT, UK
gavin@math.ucl.ac.uk

(Received 31 May 2007)

The flow of a one-and-a-half layer fluid over a three-dimensional obstacle of nondimensional height M , relative to the lower layer depth, is investigated in the presence of rotation, the magnitude of which is measured by a nondimensional parameter B (inverse Burger number). The transcritical regime in which the Froude number F , the ratio of the flow speed to the interfacial gravity wave speed, is close to unity is considered in the shallow water (small aspect ratio) limit. For weakly rotating flow over a small isolated obstacle ($M \rightarrow 0$) a similarity theory is developed in which the behaviour is shown to depend on the parameters $\Gamma = (F - 1)M^{-2/3}$ and $\nu = B^{1/2}M^{-1/3}$. The flow pattern in this regime is determined by a nonlinear equation in which Γ and ν appear explicitly, termed here the ‘rotating transcritical small disturbance equation’ (rTSD equation, following the analogy with compressible gas dynamics). The rTSD equation is forced by ‘equivalent aerofoil’ boundary conditions specific to each obstacle. Several qualitatively new flow behaviours are exhibited, and the parameter reduction afforded by the theory allows a (Γ, ν) regime diagram describing these behaviours to be constructed numerically. One important result is that, in a supercritical oncoming flow in the presence of sufficient rotation ($\nu \gtrsim 2$), hydraulic jumps can appear downstream of the obstacle even in the absence of an upstream jump. Rotation is found to have the general effect of increasing the amplitude of any existing downstream hydraulic jumps and reducing the lateral extent and amplitude of upstream jumps. Numerical results are compared with results from a shock-capturing shallow water model, and the (Γ, ν) regime diagram is found to give good qualitative and quantitative predictions of flow patterns at finite obstacle height (at least for $M \lesssim 0.4$). Results are compared and contrasted with those for a two-dimensional obstacle or ridge, for which rotation also causes hydraulic jumps to form downstream of the obstacle and acts to attenuate upstream jumps.

1. Introduction

A transcritical flow over topography can be loosely defined to occur when the topographic forcing acts to (near)-resonantly excite a significant free wave mode of the flow. In single layer flow, or equivalently the one-and-a-half layer flow to be examined in this work, transcritical flow occurs when the Froude number, or ratio of the upstream flow speed to the appropriate long gravity wave speed, is near unity. The result of the resonant excitation is the generation of nonlinear waves, whether in the form of hydraulic jumps, if the system is regularised by dissipation as in the standard shallow water treatment, or in the form of nonlinear dispersive waves and solitons in flows where dispersive effects dominate (e.g. Baines 1995, and refs. therein). An essentially analogous phenomenon is known to occur in stratified shear flow when the flow speed is comparable to the phase speed

of a significant vertically trapped free mode of the system (Grimshaw & Smyth 1986). Developing understanding of the transcritical flow regime is of particular importance, as it is the regime in which maximum drag is exerted on the flow by the obstacle, and the treatment of vertically trapped (or horizontally propagating) waves in atmospheric gravity wave drag parameterisation schemes is known to be relatively simplistic, as discussed by Lott & Miller (1997). Scale analysis reveals that transcritical flow is likely to be ubiquitous in the ocean and atmosphere (e.g. Rottman & Einaudi 1993), and characteristic transcritical flow patterns have been distinguished in cloud photographs (Stevenson 1980; Burk & Haack 1999), and by synthetic aperture radar (Li *et al.* 2004).

An established model for the study of transcritical effects is that of single layer shallow water flow. For non-rotating flow over a two-dimensional obstacle, analysis of the nonlinear shallow water model has a long history (e.g. Long 1954, 1970; Houghton & Kasahara 1968), and great utility derives from the relatively simple picture of hydraulic control that emerges. Regime diagrams can be constructed as a function of Froude number and obstacle height illustrating the possible flow configurations (e.g. Baines 1995), an approach that will be followed below. For the case of non-rotating flow over three-dimensional, isolated obstacles, a series of numerical studies (e.g. Schär & Smith 1993a,b; Jiang & Smith 2000) have allowed the construction of similar regime diagrams classifying the resulting flow patterns and behaviours. The well-known analogy with compressible gas dynamics is particularly helpful for this problem, and Jiang & Smith (2000) identify ‘bow shocks’ and ‘V-waves’ which also appear in the flow of a compressible gas over an aerofoil. This analogy has been made explicit in Esler *et al.* (2007, ERJ07 hereafter), where transcritical shallow water flow over a small isolated obstacle is shown to be isomorphic to the flow of a compressible gas around a thin ‘equivalent’ aerofoil, in the transonic small disturbance limit (e.g. Chapman 2000). The ‘equivalent aerofoil’ method of ERJ07 leads to a parameter reduction; for a given obstacle, the resulting flow depends only on a ‘transcritical similarity parameter’, a measure of the criticality of the flow relative to the topographic forcing. A similar approach will be followed below.

On the geophysical ‘mesoscale’ associated with atmospheric flow around isolated islands or over mountain ranges, rotation becomes important in determining flow patterns and drag. In the transcritical regime, rotation becomes important when the Rossby radius of deformation becomes comparable to the transverse scale of the obstacle wake, which may be much larger than the horizontal scale of the obstacle itself. This indicates a strong sensitivity of transcritical flows to even ‘weak’ rotation. One aspect is that the waves generated by topographic forcing in the presence of rotation will be distinct from those in non-rotating flow; in one-dimensional shallow water these will be nonlinear inertia-gravity waves (e.g. Shrira 1986; Grimshaw *et al.* 1998; Zeitlin *et al.* 2003), which are known to be modified by dispersion (Ostrovsky 1978). The generation of these inertia-gravity waves in the relatively simple context of flow over a two-dimensional obstacle in the presence of rotation has been studied previously (Baines & Leonard 1989; Esler *et al.* 2005). Some basic qualitative effects of rotation in the transcritical regime are apparent from these studies; upstream propagating hydraulic jumps are arrested a finite distance ahead of the obstacle, the amplitude of these jumps decreases, and a hydraulic jump appears downstream of the obstacle when the amplitude of the wave-train of inertia-gravity waves excited downstream exceeds a limiting value. In Esler *et al.* (2005, ERJ05 hereafter), analytic solutions for the special case of a parabolic ridge are developed. New aspects of these solutions are discussed below. Rotating layerwise flow over three-dimensional obstacles has, however, received less attention overall and is the main topic of this work. Vilenski & Johnson (2004) examined rotating flow over a Gaussian obstacle that is asymptotically elongated in the cross-stream direction, identifying several

representative flow patterns in the (dispersive) rotating Kadomtsev-Petviashvili equation (Kadomtsev & Petviashvili 1970). The problem of transcritical rotating flow over isolated three-dimensional (e.g. axisymmetric) obstacles has not yet been addressed, however - in particular the question of determining the explicit relationship between different steady flow regimes and the physical parameters describing the problem.

The influence of rotation on transcritical flows can also be investigated experimentally. Fig. 1 shows the interface displacement recorded during towing tank experiments (Johnson *et al.* 2006) performed at the LEGI-Coriolis rotating tank facility in Grenoble. In the experiments, a surface-mounted obstacle is towed across the tank, exciting internal waves at the interface between two layers of fluid of contrasting density. Fig. 1 (left) shows the interface elevations for an oblong obstacle towed at 10cm s^{-1} in the absence of rotation. The right hand panel shows a similar experiment, but with the tank rotating with period 120s, giving a Rossby radius of about 1m. The experimental values of the nondimensional parameters introduced above are approximately $F = 1.1 - 1.3$, $M = 0.5$ and $B = 0.5$ (in the rotating case), where the Froude number estimate is partly informed by comparing flow patterns in a number of experiments at different towing speeds with the flow patterns in the model calculations of Johnson *et al.* (2006). Appreciable differences are apparent between the non-rotating and rotating flows. In the absence of rotation (left panel), a steady bow-wave several metres in lateral extent is generated ahead of the obstacle (labelled C_1), followed by a smaller bow wave (C_{1b}) and a trough (T_1) to the rear. The basic bow-wave structure is well captured in non-dispersive (shallow water) numerical simulations (e.g. Jiang & Smith 2000), and representative model equations that include dispersive effects can predict further qualitative details of the flow pattern (e.g. Johnson & Vilenski 2004; Johnson *et al.* 2006). In rotating flow (right panel) the bow wave (C_1) is significantly decreased in lateral extent, and the secondary wave (C_{1b}) is absent. Behind this a broad trough (T_1) is still present, but immediately behind the trough, downstream of the obstacle, a large amplitude, narrow, nonlinear wave (C_2) appears. The appearance of this wave can be attributed to the rotation, and a central purpose of this work is to demonstrate that amplification of nonlinear downstream disturbances such as C_2 , and the decrease in amplitude and cross-stream extent of the bow wave (C_1) are characteristic features of rotating transcritical flow. Shallow water flows over both two and three-dimensional obstacles are described in order to demonstrate the robustness of this effect.

Section 2 presents a theoretical treatment of transcritical rotating shallow water flow over both two-dimensional obstacles, re-examining the results of ERJ05, and three dimensional obstacles, extending and developing the ‘equivalent aerofoil’ analysis of ERJ07 to include rotation. It is shown that in both cases, for relatively small obstacle height, flows are well-characterised in terms of ‘similarity parameters’ that measure the importance of criticality and rotation relative to the topographic forcing. A regime diagram is constructed for the two-dimensional results in terms of these parameters, and a nonlinear equation, the ‘rotating transcritical small disturbance (rTSD) equation’, is derived to describe the three-dimensional flows. In section 3 numerical solutions of the rTSD equation are used to construct a regime diagram describing the different flow behaviours for the three-dimensional obstacle case. The effect of rotation on the drag exerted by the obstacle on the flow is discussed. In section 4 numerical solutions of the rotating shallow water solutions are used to evaluate the accuracy of the rTSD asymptotic theory, and to verify the persistence of the rTSD flow regimes, at finite obstacle height. Section 5 gives some conclusions.

2. Similarity theories for transcritical rotating flows

2.1. Physical scenario and model equations

From a geophysical perspective, the relevant physical scenario to be modelled is that of a one-and-a-half layer inviscid fluid, consisting of a layer of undisturbed depth H and uniform density ρ_2 underlying a less dense layer (density ρ_1) of infinite vertical extent. For ease of exposition the density difference is taken to be small, hence $(\rho_2 - \rho_1)/\rho_2 \ll 1$ and the Boussinesq approximation can be made. The fluid, acted on by gravity g , rotates at angular frequency $f/2$ and both layers flow with an initially uniform horizontal speed U over an obstacle with maximum height h_m and horizontal scale L . Further, the aspect ratio of the flow is taken to be small ($H/L \ll 1$) so that shallow water dynamics applies in the lower dynamically active layer, and to leading order the flow remains uniform in the upper layer for all time.

It is straightforward to show that the non-dimensional rotating shallow water equations hold for the lower layer flow, i.e.

$$\begin{aligned} u_t + (u - F)u_x + vv_y - \sqrt{B}v &= -\sigma_x - Mh_x, \\ v_t + (u - F)v_x + vv_y + \sqrt{B}u &= -\sigma_y - Mh_y, \\ \sigma_t + [(u - F)\sigma]_x + [v\sigma]_y &= 0, \end{aligned} \quad (2.1)$$

where σ is the layer thickness, $h = h(x, y)$ is the topography, and the total horizontal velocity is $\mathbf{u} = (-F + u, v)$. The equations have been nondimensionalised by taking the horizontal length scale to be L , the horizontal velocity scale to be $c \equiv \sqrt{g'H}$ (the long interfacial gravity wave speed in the absence of rotation), the timescale to be L/c , and the layer thickness scale to be H . Three non-dimensional parameters now appear explicitly in (2.1): the Froude number $F = U/c$; the non-dimensional obstacle height $M = h_m/H$; and an inverse Burger number $B = f^2 L^2 / c^2$. Note that B is the square of the ratio of the obstacle length scale L to the radius of deformation $L_R = c/f$. Results are presented in terms of F , M , and B , or similarity parameters explicitly related to them, in all that follows.

As discussed in ERJ05, equations (2.1) apply also to an ‘experimental scenario’ in which an obstacle is towed through a single layer of rotating fluid which is otherwise at rest. However, because the single-layer rotating shallow water equations are not Galilean invariant, the set (2.1) does not apply directly to single-layer flow over an obstacle. In single layer flow, when rotation is present, the free surface must slope in order to geostrophically ‘balance’ a steady current.

In order to model the physical situation of breaking waves, solutions of (2.1) are typically regularised by including the possibility of mass and (lower layer) momentum conserving hydraulic jumps (Klemp *et al.* 1997). The idea that rotation should not significantly affect hydraulic jumps is due to Houghton (1969), who argues that since a hydraulic jump may be considered to take place across a very short distance compared to the Rossby radius of deformation ($L_R = c/f$), rotation may be considered to have a negligible effect on its internal dynamics. In two dimensions, therefore, hydraulic jumps satisfy those conditions applicable to the non-rotating system, namely

$$\begin{aligned} -V[\sigma]_{\pm}^{\pm} + [\sigma \mathbf{u} \cdot \mathbf{n}]_{\pm}^{\pm} &= 0, \\ -V[\sigma \mathbf{u} \cdot \mathbf{n}]_{\pm}^{\pm} + [\sigma(\mathbf{u} \cdot \mathbf{n})^2 + \frac{1}{2}\sigma^2]_{\pm}^{\pm} &= 0, \end{aligned} \quad (2.2)$$

where \mathbf{n} is a horizontal unit vector normal to the jump, V is the jump velocity in the direction of \mathbf{n} , and $[\cdot]_{\pm}^{\pm}$ denotes the difference between the evaluated quantity in brackets upstream and downstream of the jump. Note that in stipulating the jump conditions (2.2),

there is an implicit assumption that an unspecified dissipation acts on the (unresolved) horizontal scale of the jumps (see e.g. Jiang & Smith 2000), and therefore the full system does not conserve energy when jumps are present.

2.2. Two-dimensional obstacles

First, we present a novel summary of the theory for rotating flow over a two-dimensional obstacle, or ridge, $h = h(x)$. The two-dimensional (y -independent) version of the problem formulated above has been addressed numerically by Baines & Leonard (1989), and more recently by ERJ05. In ERJ05 the specific case of a parabolic obstacle of the form

$$h(x) = \begin{cases} 4x(1-x) & 0 < x < 1, \\ 0 & x \leq 0, x \geq 1 \end{cases}$$

is addressed in detail, as for this particular obstacle analytic progress is possible. Seeking y -independent steady solutions of (2.1), the layer thickness σ is found to satisfy

$$\left(\sigma + \frac{F^2}{2\sigma^2} \right)_{xx} + B(1 - \sigma) = -Mh_{xx}. \quad (2.3)$$

For the particular case of the parabola, equation (2.3) may be integrated and various deductions can be made about the form of the solution for given F , M and B , including the possible locations of steady hydraulic jumps, which, from (2.2), must satisfy

$$\left[\frac{\sigma^2}{2} + \frac{F^2}{\sigma} \right]_{-}^{+} = 0, \quad \left[\sigma_x \left(1 - \frac{F^2}{\sigma^3} \right) \right]_{-}^{+} = 0.$$

The results of ERJ05 are valuable for interpreting the results to be presented below for rotating flow over isolated three-dimensional obstacles. In particular, we would like to establish whether rotation has a robust, predictable effect on the flow patterns in transcritical flows, that persists regardless of the geometry of the obstacle. To make the comparison with the three-dimensional results below as straightforward as possible, a new presentation of the ERJ05 results follows. Although the ERJ05 results are valid for all values of (M, F, B) , a particularly compact and useful way of presenting the results for small M is to find similarity parameters which entirely determine the flow pattern in the limit $M \rightarrow 0$. Writing

$$\bar{\Gamma} = \frac{F-1}{M^{1/2}}, \quad \bar{\nu} = \frac{B^{1/2}}{M^{1/4}}, \quad (2.4)$$

and setting $\sigma = 1 + M^{1/2}\phi$ reduces equation (2.3), at leading order in M , to

$$\left(-2\bar{\Gamma}\phi + \frac{3}{2}\phi^2 \right)_{xx} - \bar{\nu}^2\phi = -h_{xx}. \quad (2.5)$$

Equation (2.5) describes the leading order nonlinear behaviour of the steady flow solutions of (2.3) in the weakly-rotating transcritical limit $M, B \rightarrow 0$, $F \rightarrow 1$, in which $\bar{\Gamma}, \bar{\nu}$ remain finite. For small M the problem is thus seen to be characterised by the two similarity parameters $(\bar{\Gamma}, \bar{\nu})$, and it is therefore useful to present the results of the ERJ05 study in terms of these parameters, particularly as a similar approach is taken for the three-dimensional obstacle analysis described below.

Fig. 2 shows the regime boundaries dividing the different qualitative flow behaviours found by ERJ05, presented as a function of the similarity parameters $(\bar{\Gamma}, \bar{\nu})$. The qualitative behaviours themselves are shown in the insets on the right (note that DRJ is ‘downstream recovery jump’ and that the numbering and flow direction has been changed from that in ERJ05, for consistency with the following section). The labelled curves S_1

and S_2 on the supercritical side ($\bar{\Gamma} > 0$) are derived from the formulae (19) and (21) in ERJ05; in the weakly nonlinear ($M \rightarrow 0$) case these can be shown to reduce to

$$\bar{\nu}^2 = 6 \left(\frac{9 - 6\bar{\Gamma}^2}{\bar{\Gamma}^3} \right), \quad \bar{\nu}^2 = \frac{6}{5} \left(\frac{9 - 6\bar{\Gamma}^2}{\bar{\Gamma}^3} \right),$$

respectively. The remaining curve on the supercritical side, dividing regions V and VI, and the curves on the subcritical side ($\bar{\Gamma} < 0$) are derived from numerical solution of the appropriate systems of nonlinear equations outlined in ERJ05.

Fig. 2a shows the regime diagram in the weakly nonlinear ($M \rightarrow 0$) limit. The $\bar{\nu} = 0$ axis corresponds to nonrotating flow which is characterised by transitions between regimes I and IIb, and between regimes IV and VI, at $\bar{\Gamma} = \pm\sqrt{3/2}$ respectively, (see e.g. Baines 1995). With increasing rotation the range of $\bar{\Gamma}$ for which transcritical flows (regimes II-IV) occur is seen to decrease. New sub-regimes in which the hydraulic jumps move onto the obstacle itself can now be identified in both subcritical (regime IIa) and supercritical (regime IVb) oncoming flow. For $\bar{\nu} \gtrsim 2$, a further possible regime appears for supercritical oncoming flow. In regime V, a hydraulic jump is present downstream of the obstacle, notwithstanding the complete absence of an upstream hydraulic jump.

To demonstrate that the weakly nonlinear description remains qualitatively useful in practise even at finite M , Fig. 2b shows the $(\bar{\Gamma}, \bar{\nu})$ regime diagram for $M = 0.4$. In non-rotating flow ($\bar{\nu} = 0$) some significant differences are apparent between the $M = 0.4$ and weakly nonlinear situations, as expected from Baines (1995). First, in subcritical oncoming flow, jumps may now appear on the downstream side of the obstacle (regime IIa) in non-rotating flow. Second, a region of hysteresis (IV/VI) for supercritical oncoming flow in which either a purely supercritical flow (VI) or a transcritical flow with an upstream jump (IV) may develop, depending on the flow initial conditions (see e.g. Baines & Davies 1980). One of the main results of ERJ05 is that rotation acts to suppress supercritical hysteresis, as can be seen in Fig. 2b, since the region of hysteresis disappears for $\bar{\nu} \gtrsim 2.25$. In fact for $\bar{\nu}$ greater than this value, the $M = 0.4$ regime diagram is very similar to its weakly nonlinear counterpart ($M \rightarrow 0$). In ERJ05 it was shown that hysteresis is present only for $B < 8M$, i.e. $\bar{\nu} < 8^{1/2}M^{1/4}$. At larger values of M , therefore, the hysteresis region occupies a progressively larger proportion of the corresponding $(\bar{\Gamma}, \bar{\nu})$ diagram.

The above results are specific to the parabolic obstacle. However, numerical calculations (not shown) have been used to verify that flows over other obstacles exhibit similar behaviour. Specifically, a qualitatively similar regime diagram was derived for a ‘Witch of Agnesi’ obstacle with cross-section $h(x) = 1/(1 + \pi^2 x^2)$ (the cross-sectional area of which is equal to that of the parabola above). Details of the calculations are exactly as those described in ERJ05 for the parabolic obstacle. Hence the general structure of the regime diagram Fig. 2 is likely to be generic to rotating flows over most simple two-dimensional obstacles.

2.3. Three-dimensional obstacles

The above results will now be compared with those for flow over three-dimensional isolated obstacles, again in the transcritical regime for small obstacle height M and Froude number F is close to one. The analysis loosely follows that in ERJ07, for the case of non-rotating weakly dispersive flow, but the introduction of rotation breaks the symmetry of the flow about the centreline $y = 0$, which requires careful consideration. The relevant scaling regime for rotating transcritical flow over an obstacle with small height $M \ll 1$ is suggested by ERJ07 and the derivation of the rotating Kadomtsev-Petviashvili equation

(Grimshaw & Melville 1989). The parameters

$$\Gamma = (F - 1)M^{-2/3}, \quad \nu = B^{1/2}M^{-1/3}, \quad (2.6)$$

remain of order unity as $M \rightarrow 0$. Following ERJ07, Γ is referred to as the transcritical similarity parameter and measures the supercriticality ($F > 1$, $\Gamma > 0$) or subcriticality ($F < 1$, $\Gamma < 0$) of the flow for a given obstacle height M . The parameter ν measures the importance of rotation in the transcritical regime. Both positive and negative values of ν are admissible depending on the sense of the rotation.

It is useful to introduce a free surface displacement

$$\eta = \sigma + Mh - 1,$$

a small parameter $\epsilon = M^{2/3}$, and to seek solutions of (2.1) that evolve on a ‘slow’ time scale $\tau = \epsilon t$. The variables (u, v) and η can be expanded in powers of $\epsilon^{1/2}$ as

$$\begin{aligned} u &= \epsilon \left(u_0 + \epsilon^{1/2}u_1 + \epsilon u_2 + \dots \right) \\ v &= \epsilon^{3/2} \left(v_0 + \epsilon^{1/2}v_1 + \epsilon v_2 + \dots \right) \\ \eta &= \epsilon \left(\eta_0 + \epsilon^{1/2}\eta_1 + \epsilon \eta_2 + \dots \right). \end{aligned} \quad (2.7)$$

Expansions (2.7) are used to match leading order asymptotic solutions of (2.1) in two separate regions defined by their cross-stream distance from the centre of the obstacle at $y = 0$.

In the inner region, which describes flow on streamlines that pass over or near the obstacle, the cross-stream co-ordinate is taken to be y . Denoting inner region variables with the superscript i and inserting the expansion (2.7) in (2.1), establishes that

$$u_0^i = \eta_0^i(x). \quad (2.8)$$

The leading order solution is therefore described by an (as yet) undetermined y -independent function $\eta_0^i(x)$, except for the leading order cross-stream velocity v_0^i . At the next order in the expansion

$$u_1^i = \eta_1^i(x, y), \quad v_{0y}^i = -h_x. \quad (2.9)$$

Integrating in y , the second condition gives

$$v_0^i(x, y) = V(x) - \int_0^y h_x(x, \hat{y}) d\hat{y}, \quad (2.10)$$

where $V(x)$ is an undetermined function, with the velocity v_0^i related to the free surface height through

$$-v_{0x}^i + \nu \eta_0^i = -\eta_{1y}^i. \quad (2.11)$$

Higher orders in the inner expansion reveal that $\eta_0^i(x)$ cannot be determined by the inner region alone. Further, the expansion becomes invalid sufficiently far from the obstacle, once $|y| \sim O(\epsilon^{-1/2})$ where higher order terms in the series expansion become comparable with those at leading order. Thus η_0^i is determined by matching with an outer region solution which is valid for $|y| \sim O(\epsilon^{-1/2})$.

The variable $Y = \epsilon^{1/2}y$ is next introduced, in order to capture the cross-stream scale on which the leading order free surface height and streamwise velocity vary in the cross-stream direction, in the outer region solution. The obstacle influences the outer region only through the boundary condition at $Y = 0$. Throughout the rest of the domain in the outer coordinates the bottom boundary is flat. In the outer region we seek far

field asymptotic solutions, denoted by superscript o , of (2.1). Introducing a ‘slow’ time variable $\tau = \epsilon t$, terms of the form

$$u_0 = u_0^o(x, Y, \tau) \quad \text{etc.}$$

are substituted into the series expansion (2.7). At leading order

$$u_0^o = \eta_0^o(x, Y), \quad (2.12)$$

and

$$v_{0x}^o = \eta_{0Y}^o + \nu \eta_0^o. \quad (2.13)$$

At the next order, u_1^o, v_1^o, η_1^o satisfy an identical set of equations to (2.12-2.13), and hence may be set to zero without loss of generality.

To obtain an equation for η_0^o we must proceed to $O(\epsilon^2)$, thereby introducing nonlinear terms. The x -momentum and continuity equations give

$$\begin{aligned} u_{2x}^o - \eta_{2x}^o &= -\nu v_0^o + \eta_{0\tau}^o - \Gamma \eta_{0x}^o + \eta_0^o \eta_{0x}^o, \\ u_{2x}^o - \eta_{2x}^o &= -v_{0Y}^o - \eta_{0\tau}^o + \Gamma \eta_{0x}^o - 2\eta_0^o \eta_{0x}^o. \end{aligned} \quad (2.14)$$

Eliminating u_2^o, η_2^o , and using relations (2.13) to eliminate terms involving v_0^o , gives

$$(2\eta_{0\tau}^o + 3\eta_0^o \eta_{0x}^o - 2\Gamma \eta_{0x}^o)_x - \nu^2 \eta_0^o + \eta_{0Y}^o = 0. \quad (2.15)$$

Equation(2.15) is the (dispersionless) rotating Kadomtsev-Petviashvili equation (Kadomtsev & Petviashvili 1970; Grimshaw & Melville 1989).

The novel component here is the derivation of the appropriate boundary condition on $Y = 0$, which is obtained by matching with the inner solution as follows. Matching between the inner and outer regions requires

$$\begin{aligned} \eta_0^i(x) &= \lim_{Y \rightarrow 0} \eta_0^o(x, Y), \\ \lim_{y \rightarrow \pm\infty} \eta_{1y}^i(x, y) &= \lim_{Y \rightarrow 0^\pm} \eta_{0Y}^o(x, Y), \\ \lim_{y \rightarrow \pm\infty} v_0^i(x, y) &= \lim_{Y \rightarrow 0^\pm} v_0^o(x, Y). \end{aligned} \quad (2.16)$$

These are satisfied if, from (2.10) and (2.11), the single condition

$$[\eta_{0Y}^o]_-^+ = \int_{-\infty}^{\infty} h_{xx}(x, \hat{y}) d\hat{y}, \quad (2.17)$$

is enforced, where the square brackets denote the difference between evaluation at $Y \rightarrow 0^+$ and $Y \rightarrow 0^-$. The centre-line interface displacement $\eta_0^i(x)$ and cross-stream velocity $V(x)$ in equation (2.10) are at this stage still unknown, and must be determined from the solution itself *a posteriori*. The system involving equation (2.15) and (2.17) is symmetric in η_0^o about $Y = 0$, and if desired can be solved in the half-plane, $Y \geq 0$. Crucially, however, (2.13) reveals that the leading order transverse velocity v_0^o is not antisymmetric about $Y = 0$, as it is in the non-rotating problem, and the cross-stream velocity $V(x)$ on the inner region centre-line $y = 0$, determined by (2.10), will in general be non-zero. Note that, whereas the leading order displacement η_0^o is unchanged under a change in sign of the rotation, the leading order transverse velocity v_0^o is reflected about $Y = 0$. As recognised by Grimshaw & Melville (1989) the implication of non-zero $V(x)$ on $y = 0$ is that, despite the superficial appearance of reflectional symmetry in surface displacement height, solving (2.15) and (2.17) for η_0^o in the half-plane does not recover the solution for flow over a half-obstacle when an infinite side-wall is present at $y = 0$. The physical reason is that in the rotating system, the presence of the wall introduces a new wave, the

Kelvin wave. The half-obstacle / sidewall problem will then have two distinct solutions depending on the sign of the rotation.

In order to exploit the numerical methods of gas dynamics to find steady solutions of (2.15), it is convenient to introduce

$$\phi(x, Y) = \int_x^\infty \eta_0^o(\hat{x}, Y) d\hat{x},$$

allowing (2.15) to be integrated to give the following system, valid in the half-plane $Y \geq 0$,

$$(-2\Gamma - 3\phi_x) \phi_{xx} - \nu^2 \phi + \phi_{YY} = 0, \quad (2.18)$$

subject to the boundary condition

$$\phi_Y(x, 0) = K_x(x) \quad \text{on } Y = 0, \quad \text{where } K(x) = \int_0^\infty h(x, \hat{y}) d\hat{y}. \quad (2.19)$$

With $\nu = 0$, this system is the transonic small disturbance equation, or Kármán-Guderley equation, for flow over a thin symmetric aerofoil with half-thickness $\epsilon K(x)$. The aerofoil shape $K(x)$ is the (half) cross-sectional area of the obstacle. For rotating flow with $\nu \neq 0$, equation (2.18) is described here as the rotating transcritical small disturbance (rTSD hereafter) equation.

For definiteness attention will be restricted in the following to two specific axisymmetric obstacles, with nondimensional radial height profiles given by

$$h(r) = \begin{cases} 1 - r^2 & r < 1, \\ 0 & r \geq 1, \end{cases} \quad \text{Paraboloid, (PB)} \quad (2.20)$$

$$h(r) = \frac{1}{(1 + 4r^2)^{3/2}} \quad \text{'Witch of Agnesi', (WA).}$$

These two obstacles represent relative extremes of behaviour, that of 'compact' and 'non-compact' obstacles respectively, found in the non-rotating study of ERJ07. The second of the two obstacles has also been studied in detail in the nonrotating context by several authors (see Schär & Smith 1993a; Jiang & Smith 2000). Note that both obstacles have maximum height unity, for consistency with the non-dimensionalisation, and have equal volume $\mathcal{V} = \pi/2$. Hence differences in flow behaviour can be attributed purely to differences in obstacle shape. The equivalent aerofoils for the two obstacles, illustrated in ERJ07 (see their Fig. 1), are

$$K(x) = \begin{cases} \frac{2}{3}(1 - x^2)^{3/2} & |x| < 1, \\ 0 & |x| \geq 1, \end{cases} \quad \text{Paraboloid, (PB)} \quad (2.21)$$

$$K(x) = \frac{1}{2(1 + 4x^2)}, \quad \text{'Witch of Agnesi', (WA).}$$

3. Transcritical rotating flows over three-dimensional obstacles in the small disturbance limit

The transcritical asymptotic theory presented above for three-dimensional obstacles reduces the three-parameter (M, F, B) problem for flow over an obstacle of finite height to a two-parameter problem (Γ, ν) that is formally valid for small obstacles, $M \ll 1$. The parameter reduction allows the numerical construction of a regime diagram describing the qualitative behaviour of transcritical rotating flow over a three-dimensional obstacle, to compare with the two-dimensional obstacle regime diagram Fig. 2a. As in the two-dimensional obstacle case, it can be expected that the regime diagram will be a reasonably

accurate guide to behaviour even at finite values of M . In fact since there is no known hysteresis behaviour for flow over simple axisymmetric three-dimensional obstacles (e.g. Baines 1995) the $M \rightarrow 0$ regime diagram may remain accurate for relatively high values of M , as is shown in section 4 below.

3.1. Numerical solution of the *rTSD*

The *rTSD* equation (2.18), with the ‘equivalent aerofoil’ boundary condition (2.19) can be solved by making relatively minor modifications to existing algorithms for the non-rotating TSD equation developed in the study of flow over aerofoils in gas dynamics (e.g. Cole & Cook 1986). The type-dependent finite difference scheme used to obtain the solutions below was developed by Murman & Cole (1971) and refined by Engquist & Osher (1980). The basic concept behind the technique is that a different finite-difference stencil is used depending on whether the flow is locally subcritical and the equation (2.18) is therefore locally elliptic (centred differences), is locally supercritical / hyperbolic (upstream sided differences), or is in transition between the two at a shock (hydraulic jump) or sonic line. The resulting difference equations are solved using the monotonic implicit approximate-factorization scheme of Goorjian & Van Buskirk (1981), with the low frequency modes damped by means of the multi-grid acceleration technique described by Jameson (1979). The inclusion of the extra rotating term in (2.18) is straightforward, and is found to have the effect of further stabilising the behaviour of all algorithms tested. For supercritical oncoming flow, the boundary conditions are $\phi_x = 0$ at the upstream boundary, with outflow conditions on the upper and downstream boundaries. For subcritical oncoming flow, in the absence of rotation, ϕ may be specified on the lateral boundaries using the anticipated asymptotic form of the far field solution to the TSD (e.g. Cole & Cook 1986). In rotating flow, the far field solution decays exponentially with distance from the aerofoil, hence it is sufficient to set $\phi = 0$ on (suitably distant) lateral boundaries.

As discussed in detail in ERJ07, there are difficulties in obtaining numerical solutions of (2.18) in a finite domain as $|\Gamma| \rightarrow 0$. In the non-rotating case the domain size needs to be extended indefinitely as this limit is approached, in order to prevent the upstream hydraulic jump from reaching the upstream boundary of the domain, as well as to prevent wave reflection from the lateral domain boundaries. Rotation alleviates these problems to an extent, although solutions with $|\Gamma|$ sufficiently close to zero remain problematic. Solutions are therefore obtained on a range of domain sizes, depending on the values of Γ and ν , from $10L \times 10\epsilon^{-1/2}L$ to $40L \times 40\epsilon^{-1/2}L$. Grid spacings vary between $\delta x = 0.05L$ (low resolution) and $\delta x = 0.01L$ (high resolution). For all of the numerical calculations, care was taken on a case-by-case basis to ensure that the flow patterns and calculated drags are unaffected by further increases in domain size, that the flow field in the vicinity of the obstacle is steady, and that adequate convergence with respect to spatial resolution has occurred.

3.2. Transcritical flows in the *rTSD* limit

Fig. 3 shows numerical solutions of the *rTSD* (2.18) for the paraboloid (PB) equivalent aerofoil boundary conditions (2.19), with $K(x)$ given by equation (2.21), at different values of the similarity parameters Γ (criticality) and ν (rotation). Recall that the equivalent aerofoil boundary conditions (2.19) represent the effect of the corresponding three-dimensional obstacle (2.20) on the flow in the *rTSD* limit, and hence in this limit the forcing from the obstacle is compressed onto the line $Y = 0$. The quantity contoured is the leading order surface displacement field $\eta_0^o(x, Y)$ ($= \phi_x$), and shaded regions are regions of embedded supercritical flow (when the oncoming flow is subcritical, $\Gamma < 0$) or

embedded subcritical flow (when the oncoming flow is supercritical, $\Gamma > 0$). Note that the rTSD solutions for $\eta_0^o(x, Y)$ are symmetric about the centreline ($Y = 0$). Shallow water flows at finite M are asymmetric about the centreline, but as will be seen below this asymmetry enters the asymptotic theory at higher order. The different panels in Fig. 3 illustrate typical flow patterns in the qualitatively different flow regimes found as Γ and ν are varied: these flow patterns are described in more detail below.

Fig. 4a gives the regime diagram for the rTSD equation in (Γ, ν) parameter space for the paraboloid obstacle. The regime boundaries are established numerically by repeatedly finding steady solutions to the rTSD equation (2.18). The regime diagram is to be examined in conjunction with Fig. 3, where the corresponding flow patterns are illustrated (note that each panel in Fig. 3 is labelled with the number of the appropriate regime). The exact location in parameter space of the Fig. 3 example solutions are marked in Fig. 4 as triangles.

In regime I the flow is entirely subcritical throughout the domain. The solution is symmetric in x and rotation is found to cause the solution to decay more rapidly away from the obstacle, causing the lateral extent of the disturbance field to be reduced relative to its non-rotating counterpart. In regime II a region of supercritical flow appears near the rear of the obstacle. Fluid is accelerated smoothly from subcritical to supercritical past the obstacle (shaded region in panel), before abruptly decelerating to subcritical via a hydraulic jump. In the regime diagram Fig. 4a, with increasing rotation the boundary between regimes I and II moves closer to $\Gamma = 0$, reducing the region of parameter space where transcritical solutions exist. Region II can be further subdivided into IIa and IIb depending on whether the embedded supercritical flow remains attached to the obstacle (IIa) or is detached (IIb, not shown). The detached (IIb) solution shows the characteristic ‘fishtail’ system of jumps behind the obstacle trailing edge characteristic of compressible gas flow over an aerofoil (see, e.g. Chapman 2000). In regime IIa the effect of rotation is sufficiently strong that the embedded region of supercritical flow lies entirely over the obstacle, and the ‘fishtail’ system of jumps is destroyed.

For supercritical oncoming flow throughout region III, the displacement field differs little from the corresponding non-rotating flows. The flow contains a single embedded region of subcritical flow, enclosing the leading edge of the obstacle, with a hydraulic jump at its upstream boundary beyond which the flow is undisturbed. Downstream of the obstacle the flow returns to its undisturbed state through a supercritical leap; supercritical leaps being distinguishable from hydraulic jumps in that they connect two regions of supercritical flow, as opposed to allowing a transition between supercritical flow and subcritical flow. In region IV, by contrast, the flow field no longer qualitatively resembles that found in non-rotating flow. An embedded region of subcritical flow enclosing the leading edge of the obstacle remains, but additional embedded regions of subcritical flow appear to the rear of the obstacle. The nature of these further regions of embedded subcritical flow allows region IV to be subdivided into IVa, IVb and IVc. In IVa two embedded regions of subcritical flow are found downstream of the obstacle on either side of the centreline $Y = 0$, seen in the shaded regions in the IVa panel of Fig. 3 to the rear of the obstacle. Note that as Γ is decreased to cross the regime boundary between regions III and IVa, these embedded subcritical regions are not found to migrate inwards from infinity, rather they first appear at a finite distance from the obstacle. At the regime boundary between IVa and IVb, the two embedded subcritical regions downstream join at $Y = 0$ to form a single region, and a broad hydraulic jump is now present to the rear of the obstacle. In the IVb panel of Fig. 3, this broad hydraulic jump forms the rear of a ‘fishtail’ system of jumps, the first of which are supercritical leaps, initiated at the obstacle trailing edge. If ν is increased towards the boundary between regions IVb and

IVc in the regime diagram, the fishtail system of jumps occupies a progressively smaller area, until the rear jump becomes attached to the rear of the obstacle in region IVc. Region IVc is therefore characterised as having hydraulic jumps attached to both edges of the obstacle, as can be seen in the IVc panel of Fig. 3.

With increasing Γ , or more supercritical oncoming flow, the strength and lateral extent of the hydraulic jump at the upstream edge of the obstacle decrease. If rotation is sufficiently strong ($\nu \gtrsim 2.5$), the upstream jump disappears altogether, defining the boundary with region V of parameter space. In region V there is no upstream jump, but a jump remains at the downstream edge of the obstacle. Region V solutions therefore no longer have a region of embedded subcritical flow enclosing the leading edge of the obstacle, although embedded regions of subcritical flow remain at the obstacle rear. The nature of these subcritical regions can be used to subdivide region V in a similar fashion to region IV, and Fig. 3 shows a typical flow from region Vb. If Γ increases further, the flow eventually becomes supercritical everywhere in region VI of parameter space. Region VI flows are characterised by supercritical leaps lying approximately along the ‘Mach lines’ emanating from the leading and trailing edges of the obstacle.

Fig. 4b shows the equivalent regime diagram for the ‘Witch of Agnesi’ (WA) obstacle. Flow regimes are labelled as for the paraboloid obstacle. For the ‘Witch of Agnesi’ obstacle, no distinction can be made between regions of embedded subcritical or supercritical flow lying on or off the obstacle, as the obstacle has no definite boundary, so there are fewer regime subdivisions. Nevertheless the regime diagram has the same main qualitative features as for the paraboloid obstacle. Perhaps the most notable difference between the two obstacles is that at relatively high rotation rates ($\nu \gtrsim 2$), the transition from regime IV solutions which have jumps both ahead of and behind the obstacle, to regime V solutions in which only the rear jump is present, occurs at much lower values of Γ for the ‘Witch of Agnesi’ obstacle. Further, the change in character of the supercritical transition noted above occurs for $\nu \sim 1.7$, significantly lower than for the paraboloid obstacle. Thus it appears that although solutions for the paraboloid and ‘Witch of Agnesi’ obstacles are qualitatively similar, the effects of rotation are felt somewhat more strongly by the ‘Witch of Agnesi’ obstacle than the paraboloid.

One of the most important aspects of the problem under investigation is to determine the effect of rotation on the drag exerted by the obstacle on the flow in the transcritical regime. As shown in ERJ07, drag in the rTSD limit is given by the drag on the ‘equivalent aerofoil’ in the rTSD solution. In terms of the model parameters, and the displacement height field, the drag is given by

$$\mathcal{D} = M^{5/3} \int_{-\infty}^{\infty} \eta_0^o(x, 0) K_x(x) dx = M^{5/3} D(\Gamma, \nu),$$

where the function $D(\Gamma, \nu)$ must be determined numerically. Fig. 5 shows the drag function $D(\Gamma, \nu)$ for fixed values of ν calculated from a series of steady numerical solutions of equation (2.18), for the paraboloid obstacle. In the non-rotating case ($\nu = 0$) the drag curve rises steeply on the subcritical side, plateaus at a fixed value, and then decays more gradually on the supercritical side. Very similar drag curves were found for four other obstacles in ERJ07. It is clear from Fig. 5 that rotation has a strong and systematic effect on the drag exerted by the obstacle on the flow: as ν increases the range of Γ for which significant drag is exerted is reduced at the subcritical end. For $\nu \gtrsim 2$ significant drag is exerted only for significantly supercritical oncoming flows ($\Gamma > 1$) and as rotation increases further the peak drag begins to decrease. At all values of ν investigated, the drag is found to approximate its nonrotating value for sufficiently high Γ . Solid circles

on each curve in Fig. 5 indicate the location of the regime boundaries of Fig. 4, and in some cases these correspond to points of inflection on the corresponding drag curve.

4. Transcritical rotating flows over finite height three-dimensional obstacles

The question naturally arises as to what extent solutions to the rTSD equation represent those of the full rotating shallow water equations. In ERJ07, the non-rotating theory was found to be reasonably accurate for $M \lesssim 0.4$ and $|\Gamma| \lesssim 1$. Can each flow regime discovered in the rTSD solutions above be identified at finite obstacle height M in solutions of the rotating shallow water equations, especially once some of the assumptions underpinning the asymptotic theory hold weakly at best? Are drag and regime boundary predictions still reasonable? These questions are addressed next.

4.1. Numerical solution of the rotating shallow water equations

The rotating shallow water equations (rSWE) are solved numerically using the CLAWPACK finite volume code (Conservation LAWs software PACKage, LeVeque 2002). CLAWPACK solves hyperbolic systems of equations, usually written in conservation form, using an algorithm due to Roe (1981) in which the global problem under investigation is first discretised into a set of local Riemann problems by assuming a piecewise discontinuous form for the solution. The set of Riemann problems are linearised following Roe's algorithm and solved using Godunov's upwind method (LeVeque 2002). The great advantage of this algorithm is that, provided the governing equations can be written in conservation form, the speed of propagation of shock discontinuities satisfying the global conservation laws is accurately captured. Here CLAWPACK is adapted to solve the shallow water equations (2.1) written in conservation form, and the relevant shock discontinuities are the hydraulic jumps (2.2). The forcing terms due to the obstacle and rotation cannot be included in the conservation form of (2.1), and are handled using Strang splitting, where the time tendency at each step is split into a contribution from the unforced equations calculated using Roe's method, and a separately computed contribution from the forcing, evaluated using standard semi-implicit finite difference methods. Rotation terms have previously been included following this technique by Kuo & Polvani (1997), and one-dimensional solutions using this algorithm have been validated against analytical solutions in ERJ05. Recent advances in finite-volume numerical schemes (Audusse *et al.* 2004; Bouchut *et al.* 2004) allow rotation to be incorporated into the equations with greater formal accuracy than the present method, nevertheless the resolution required to obtain high accuracy in the present calculations is not a limitation.

Very similar domain size problems occur for the rSWE integrations in the limit $F \rightarrow 1$ as those described above for the rTSD integrations in the limit $\Gamma \rightarrow 0$. Progressively larger domain sizes are required as the limit is approached in each case. Solutions are therefore obtained on domains ranging in size from $10L \times 10L$ to $50L \times 50L$, with grid-spacing ranging between $\delta x = 0.05L$ (low resolution) to $\delta x = 0.01L$ (high resolution). The model is integrated forwards in time with an adjustable time-step based on the Courant-Friedrichs-Lewy criterion (for details see, LeVeque 2002) until the flow in a pre-determined region around the obstacle converges to satisfy a steady state numerical criterion.

4.2. Transcritical flows in rotating shallow water

Fig. 6 shows steady height fields $\eta = \sigma - 1 + Mh$ obtained from numerical integrations of the rotating shallow water equations (2.1). The parameters (M, F, B) for each panel

are $M = 0.4$ with F and B then chosen to set Γ and ν equal to their values in the corresponding panel in Fig. 3 (see also triangles in Fig. 4). Contour intervals have been scaled by ϵ for consistency with the transcritical asymptotic theory results of Fig. 3. Note also that to facilitate direct comparison with Fig. 6, the aspect ratio in Fig. 3 has been selected to correspond to an obstacle height $M = 0.4$, i.e. a distance unit in the Y -direction is $\epsilon^{-1/2} = M^{-1/3} \approx 1.357$ times longer than a distance unit in the x -direction.

Comparison of Figs. 3 and 6 reveals that each of the different regimes identified for the rTSD solutions can be seen to persist at finite obstacle height $M = 0.4$. Further, each flow regime has been identified within the expected region of parameter space in the regime diagram constructed for the rTSD equation (Fig. 4). In most cases the rTSD solutions in Fig. 3 capture both quantitatively and qualitatively the important details of the rSWE wake shown in Fig. 6, at least away from the obstacle itself. One exception is the case of purely subcritical flow, (regime I, top left panel of Fig. 6), for which the solution to the full rotating shallow water equations is somewhat different to the corresponding rTSD solution. This disagreement arises because the disturbance to the free-surface elevation in the regime I shallow water solution is confined largely over the obstacle, whereas the rTSD solutions are formally valid only for the far-field. A further notable difference is that in regime IVa an embedded region of subcritical flow to the rear of the obstacle (shaded) exists only for $y < 0$.

The most obvious departure from the asymptotic solutions is the rather weak asymmetry of the displacement height fields about $y = 0$ seen in Fig. 6. The asymmetry enters at higher order in the asymptotic theory for the displacement height field. The asymmetry in the cross-stream velocity v , however, is captured at leading order by the rTSD, as is noted below. A further process of interest that is relegated to higher order in the rTSD approximation is that of vorticity generation by the shock itself (see e.g. Schär & Smith 1993b). Analysis of the Fig. 6 rSWE solutions reveals that this is most significant for the regime II solution, contributing to the observed asymmetry about $y = 0$, which is more pronounced than that in the other regimes.

Fig. 7 shows the drag \mathcal{D} exerted by the paraboloid obstacle on the flow, calculated from the rSWE solutions, against the Froude number F of the oncoming flow. Results are given for two different obstacle heights ($M = 0.05$ and $M = 0.4$), and are compared for constant values of the similarity parameter ν , i.e. not for the same value of the rotation parameter (inverse Burger number) B , but for the same value of $BM^{-2/3}$ ($= \nu^2$) in order to test the rTSD theory. The drag \mathcal{D} is scaled by M^2 to allow comparison between rSWE solutions at different values of M and linear predictions (dashed curves). The dashed curves are obtained from an exact linear theory of drag for which $\mathcal{D} \propto M^2$. The linear theory, which has been derived analytically, has been confirmed by comparison with the numerical model in the appropriate parameter regime; the details will be discussed elsewhere. The rTSD predictions (solid curves) are also shown in Fig. 7 for the obstacle heights $M = 0.05$ and $M = 0.4$. Note that the appropriate rTSD curve of Fig. 5 must be re-plotted for each value of M because the rTSD theory predicts that drag is proportional to $M^{5/3}$ in the rTSD limit (not M^2). The solid rTSD curves are plotted only for a finite range of Γ that encompasses the region where the rTSD theory might be expected to apply, corresponding to a finite range in F that increases as $M^{2/3}$. The transition to purely supercritical flow in the rTSD solutions is marked by a solid circle on each curve.

The top left panel shows non-rotating results ($\nu = 0$, see also ERJ07), the top right panel results for rotation rates corresponding to $\nu = 2$ and the bottom panels results for $\nu = 5$. Note that the bottom right panel repeats the results for $\nu = 5$, but zooming in on the dotted rectangle from the left hand panel, to illustrate the behaviour close to

$F = 1$ for the $M = 0.4$ solutions. In each panel, the rSWE drags are plotted as triangles ($M = 0.05$) and squares ($M = 0.4$). The rSWE drag curves follow the solid rTSD drag curves close to $F = 1$ before joining the dashed linear drag curves at higher values of F . As expected, the $M = 0.05$ results adhere more closely to the rTSD asymptotic predictions than the $M = 0.4$ results. At higher values of ν , linear theory is accurate for a greater range of Froude numbers F , whilst the range of F for which the rTSD accurately predicts the rSWE drag is decreased. The results for the case with $M = 0.05$ and $\nu = 5$ in fact show that linear theory accurately describes the drag at all values of F , and the rTSD and linear drags almost coincide for $F \in [1, 1.2]$. For $M = 0.4$ and $\nu = 5$ (bottom right panel), by contrast, the rTSD theory predicts the drag much better within the range $F \in [1, 1.5]$, with linear theory being more accurate for $F > 1.5$. To summarise, a useful rule to estimate drag over a finite obstacle up to $M = 0.4$, for all values of F and all rotation rates, is simply to take the minimum of the rTSD drag prediction $D(\Gamma, \nu)M^{5/3}$ and the calculated linear drag.

To examine in more detail the breakdown of the weakly nonlinear rTSD theory as a function of M , the location in obstacle height - Froude number (M, F) parameter space of the transitions from purely subcritical / supercritical flow to transcritical flow has been calculated from the rTSD results for both nonrotating flow ($\nu = 0$) and rotating flow ($\nu = 2$). Fig. 8 shows the calculated regime diagrams for the paraboloid obstacle. The region of parameter space labelled SPC corresponds to entirely supercritical flows, the entirely subcritical flow regime is labelled SBC and the transcritical flow regime TC. The locations in (M, F) space where transition occurs in the numerical calculations are labelled with stars. The predictions from the rTSD equation, which are expected to be accurate for small M , are plotted as solid curves. The rTSD theory can be seen in Fig. 8 to predict these transitions accurately at finite M particularly in rotating flows. The dotted curves show the corresponding results, valid for all M but particular to the case of a parabolic obstacle, for the case of one-dimensional flow over a ridge discussed in section 2.2.

As noted in section 2, one feature of the rTSD asymptotic theory is that, although the free surface displacement η and streamwise velocity u fields are symmetric in Y at leading order, the leading order cross-stream velocity v is not anti-symmetric about $Y = 0$ (as it would be in non-rotating flow). Fig. 9 compares the leading order v diagnosed from an rTSD solution (using equation 2.13, upper panels) with that from the corresponding rSWE solution for the $M = 0.4$ obstacle (lower panels). Note that contour intervals and the Y -scale for the rTSD solution have been chosen to allow direct comparison with an $M = 0.4$ rSWE solution. The surface displacement fields for the same flows can be compared in the ‘regime IVb’ panels of Figs. 3 and 6 respectively. The results show that the rTSD asymptotic theory captures the main asymmetric structure of the v field away from the obstacle in the full rSWE solution. The upper right and lower right hand panels show cross sections of the transverse velocity v along $y = 1$ (solid line) and $y = -1$ (dashed line) for the rTSD and rSWE respectively. Results have again been scaled for consistency with the transcritical asymptotic theory, and show that the changes in v at the hydraulic jumps have again been captured by the rTSD theory, although the rear jumps are somewhat smaller in amplitude in the rSWE case, due to the proximity of the obstacle.

5. Conclusions

One-and-a-half layer rotating flow over topography is, in the shallow water or small aspect ratio limit, fully described by three parameters: M (non-dimensional obstacle

height), F (upstream Froude number) and B (inverse Burger number). The results presented here reveal that in the transcritical regime ($F \sim 1$), for sufficiently small M , a parameter reduction is possible that allows the flow to be described by just two ‘similarity parameters’ that measure the relative importance of criticality and rotation relative to topographic forcing. In transcritical flow the effective topographic forcing varies with $M^{1/2}$ in flow over a 2D obstacle and with $M^{2/3}$ for flow over a 3D obstacle, and the relevant similarity parameters are therefore found to be $\{\bar{\Gamma} = (F - 1)M^{-1/2}, \bar{\nu} = B^{1/2}M^{-1/4}\}$ and $\{\Gamma = (F - 1)M^{-2/3}, \nu = B^{1/2}M^{-1/3}\}$ respectively.

Regime diagrams describing the qualitative flow behaviour as a function of the similarity parameters have been constructed for both 2D and 3D obstacles (Figs. 2 and 4). These reveal that rotation has remarkably similar effects despite the very different flow geometries. For example, rotation is found to have a robust tendency to generate and / or amplify hydraulic jumps found downstream of the obstacle. The physical reason for the existence of these downstream jumps in rotating flow relates to the fact that a ‘limiting amplitude’ exists for inertia-gravity waves generated downstream of the obstacle (Shrira 1986; Grimshaw *et al.* 1998). If the topographic forcing exceeds that required to generate a wavetrain of limiting amplitude, then a hydraulic ‘recovery’ jump appears downstream within a single wavelength of the obstacle, and following the recovery jump are waves at or below the limiting amplitude. Additionally, rotation acts to decrease the amplitude of upstream hydraulic jumps, and for flow over a 3D obstacle also their lateral extent. For $\bar{\nu} \gtrsim 2$ (2D obstacles) or $\nu \gtrsim 2$ (3D obstacles) the nature of the supercritical transition is found to change qualitatively, with hydraulic jumps first appearing to the rear of the obstacle as the Froude number is reduced, rather than appearing upstream as in non-rotating flow. For both the 2D and 3D obstacles the presence of rotation also reduces the range of subcritical flows for which hydraulic jumps are found. However, one important qualitative difference between the 2D and 3D obstacle cases remains the presence of supercritical hysteresis, which occurs in non-rotating flow over 2D obstacles (e.g. Baines & Davies 1980) as well as at low rotation rates (e.g. ERJ05), but has not been discovered to occur for flow over axisymmetric 3D obstacles (e.g. ERJ07). Note that supercritical hysteresis does not exist in the weakly nonlinear limit ($M \rightarrow 0$) and hence is not captured by the reduction to the similarity parameters. This is a limitation of the similarity theory, albeit one that applies only to the 2D obstacle flows.

Drag predictions from the rTSD theory, together with a theory for linear supercritical drag, combine to offer a reasonably complete description of the drag in the 3D obstacle problem. A useful rule is found to be that the drag on a finite obstacle is given to a reasonable approximation by the minimum of the rTSD and linear predictions. In the transcritical regime rotation reduces the range of Froude numbers for which drag is large. When rotation is strong, non-zero drag occurs only for significantly supercritical oncoming flows. These results may provide useful insight for the design of orographic gravity wave drag schemes for numerical weather prediction and climate models.

In the towing tank experiments of Fig. 1, rotation was also observed to attenuate the amplitude and lateral extent of the upstream nonlinear ‘bow’ wave and to generate a nonlinear wave downstream of the obstacle, just as in the rSWE results above. However, dispersive effects are clearly important in the towing tank experiments, not least because the observed disturbances resemble solitary waves rather than hydraulic jumps. Dispersion can be straightforwardly incorporated into the asymptotic transcritical theory given here, following ERJ07. If the dispersive effects enter as for a single layer of fluid, equation

(2.15) becomes,

$$\left(2\eta_{0\tau}^o + 3\eta_0^o\eta_{0x}^o - 2\Gamma\eta_{0x}^o + \frac{\Delta^2}{3}\eta_{0xxx}^o\right)_x - \nu^2\eta_0^o + \eta_{0YY}^o = 0, \quad (5.1)$$

with the ‘equivalent aerofoil’ boundary condition (2.17) unchanged. Here the dispersion parameter $\Delta = \delta M^{-1/3}$, where $\delta = H/L$ is the relevant aspect ratio (layer depth divided by horizontal obstacle scale). Comparison of solutions of (5.1) and shallow water results in the non-rotating case, given in ERJ07, reveal that solitary waves often replace hydraulic jumps in exactly the same location. Perhaps it is unsurprising that in the towing tank experiments and in the current numerical investigation, rotation is thus seen to affect non-dispersive and dispersive flows in similar ways. Further numerical exploration of the behaviour of (5.1) is described elsewhere (Vilenski & Johnson 2004), and steady solutions of a variant of (5.1) with dispersion of Benjamin-Davis-Acrivos type, appropriate for a one-and-a-half layer fluid (Benjamin 1967; Davis & Acrivos 1967), are presented in Johnson *et al.* (2006).

Transcritical rotating flow patterns may be observable in a wider range of geophysical scenarios than those detailed above. A detailed understanding of the transcritical regime may therefore be necessary in order to accurately parameterise mountain drag in some climatological situations. Future rotating tank experiments will be of interest to determine how readily different steady flow regimes establish themselves, and to investigate the transitions between them.

Acknowledgments

ERJ and OJR acknowledge funding from the UK Natural Environmental Research Council through grant no. NER/A/S/2000/01323 and research studentship NER/S/A/2003/11387.

REFERENCES

- AUDUSSE, E., BOUCHUT, F., BRISTEAU, M.-O., KLEIN, R. & PERTHAME, B. 2004 A fast and stable well-balanced scheme with hydrostatic reconstruction for shallow water flows. *SIAM J. Sci. Comp.* **25**, 2050.
- BAINES, P. G. 1995 *Topographic Effects in Stratified Flows*. Cambridge: Cambridge University Press.
- BAINES, P. G. & DAVIES, P. A. 1980 *Laboratory studies of topographic effects in rotating and/or stratified fluids*, chap. 8, p. 233. World Meteorological Organization GARP.
- BAINES, P. G. & LEONARD, B. P. 1989 The effects of rotation on flow of a single layer over a ridge. *Q. J. R. Meteorol. Soc.* **115**, 293.
- BENJAMIN, T. 1967 Internal waves of permanent form in fluids of great depth. *J. Fluid Mech.* **29**, 559–592.
- BOUCHUT, F., LE SOMMER, J. & ZEITLIN, V. 2004 Frontal geostrophic adjustment and non-linear wave phenomena in one-dimensional rotating shallow water. Part II. High resolution numerical simulations. *J. Fluid Mech.* **514**, 35–63.
- BURK, S. D. & HAACK, T. 1999 The dynamics of wave clouds upwind of coastal orography. *Mon. Weather Rev.* **28**, 1438–1455.
- CHAPMAN, C. J. 2000 *High Speed Flow*. Cambridge: Cambridge University Press.
- COLE, J. D. & COOK, P. 1986 *Transonic Aerodynamics*. New York: North-Holland.
- DAVIS, R. E. & ACRIVOS, A. 1967 Solitary internal waves in deep water. *J. Fluid Mech.* **29**, 593–607.
- ENGQUIST, B. & OSHER, S. 1980 Stable and entropy satisfying approximations for transonic flow calculations. *Math. Comp.* **34**, 45–75.
- ESLER, J. G., RUMP, O. J. & JOHNSON, E. R. 2005 Steady rotating flows over a ridge. *Phys. Fluids* **17**, 116601.
- ESLER, J. G., RUMP, O. J. & JOHNSON, E. R. 2007 Nondispersive and weakly dispersive single layer flow over an axisymmetric obstacle: The equivalent aerofoil formulation. *J. Fluid Mech.* **574**, 209–237.
- GOORJIAN, P. M. & VAN BUSKIRK, R. 1981 Implicit calculations of transonic flows using monotone methods. *AIAA Paper* **81**, 331.
- GRIMSHAW, R. H. J. & MELVILLE, W. K. 1989 On the derivation of the modified Kadomtsev-Petviashvili equation. *Stud. Appl. Math.* **80**, 183–203.
- GRIMSHAW, R. H. J., OSTROVSKY, L. A., SHRIRA, V. I. & A., S. Y. 1998 Long nonlinear surface and internal gravity waves in a rotating ocean. *Surveys in Geophysics* **19**, 289–338.
- GRIMSHAW, R. H. J. & SMYTH, N. 1986 Resonant flow of a stratified fluid over topography. *J. Fluid Mechanics* **169**, 429–464.
- HOUGHTON, D. D. 1969 Effect of rotation on the formation of hydraulic jumps. *J. Geophys. Res.* **74**, 1351.
- HOUGHTON, D. D. & KASAHARA, A. 1968 Nonlinear shallow fluid flow over an isolated ridge. *Comm. Pure Appl. Math.* **21**, 1.
- JAMESON, A. 1979 Acceleration of transonic potential flow calculations on arbitrary meshes by the multiple grid method. *AIAA Paper* **79**, 1458.
- JIANG, Q. & SMITH, R. B. 2000 V-waves, bow shocks, and wakes in supercritical hydrostatic flow. *J. Fluid Mech.* **406**, 27–53.
- JOHNSON, E. R., ESLER, J. G., RUMP, O. J., SOMMERIA, J. & VILENSKI, G. G. 2006 Orographically generated nonlinear waves in rotating and nonrotating two-layer flow. *Proc. Roy. Soc. Lond. Ser. A.* **462**, 3–20.
- JOHNSON, E. R. & VILENSKI, G. G. 2004 Flow patterns and drag in near-critical flow over isolated orography. *J. Atmos. Sci.* **61**, 2909–2918.
- KADOMTSEV, B. B. & PETVIASHVILI, V. I. 1970 On the stability of solitary waves in weakly dispersing media. *Sov. Phys. Dokl.* **15**, 539–541.
- KLEMP, J. B., ROTUNNO, R. & SKAMAROCK, W. C. 1997 On the propagation of internal bores. *J. Fluid Mech.* **331**, 81–106.
- KUO, A. & POLVANI, L. M. 1997 Time-dependent fully nonlinear geostrophic adjustment. *J. Phys. Ocean.* **27**, 1614.

- LEVEQUE, R. J. 2002 *Finite Volume methods for Hyperbolic Problems*. Cambridge: Cambridge University Press.
- LI, X. F., DONG, C. M., CLEMENTE-COLON, P., PICHEL, W. G. & FRIEDMAN, K. S. 2004 Synthetic aperture radar observation of the sea surface imprints of up-stream atmospheric solitons generated by flow impeded by an island. *J. Geophys. Res.* **209**, 10.1029.2003JC002168.
- LONG, R. R. 1954 Some respects of the flow of stratified fluids, II. Experiments with a two-layer system. *Tellus* **6**, 97.
- LONG, R. R. 1970 Blocking effects in flow over obstacles. *Tellus* **22**, 471.
- LOTT, F. & MILLER, M. J. 1997 A new sub-grid scale orographic drag parameterization: Its formulation and testing. *Q. J. R. Meteorol. Soc.* **123**, 101–127.
- MURMAN, E. M. & COLE, J. D. 1971 Calculations of plane steady transonic flows. *AIAA Journal* **9**, 114–121.
- OSTROVSKY, L. A. 1978 Nonlinear internal waves in a rotating ocean. *Oceanology* **18**, 181–191.
- ROE, P. L. 1981 Approximate Riemann solvers, parameter vectors, and difference schemes. *J. Comput. Phys.* **43**, 357–372.
- ROTTMAN, J. W. & EINAUDI, F. 1993 Solitary waves in the atmosphere. *J. Atmos. Sci.* **50**, 2116–2136.
- SCHÄR, C. & SMITH, R. B. 1993a Shallow water flow past an isolated topography. Part I: Vorticity production and wake formation. *J. Atmos. Sci.* **50**, 1373–1400.
- SCHÄR, C. & SMITH, R. B. 1993b Shallow water flow past an isolated topography. Part II: Transition to vortex shedding. *J. Atmos. Sci.* **50**, 1401–1412.
- SHRIRA, V. I. 1986 On long strongly nonlinear waves in a rotating ocean. *IAP0* **22**, 298–305.
- STEVENSON, R. E. 1980 The 200-mile fishline. In *Oceans from Space* (ed. P. C. Badgley, L. Miloy & L. Childs). Houston: Gulf Publishing Company.
- VILENSKI, G. G. & JOHNSON, E. R. 2004 Near critical free-surface rotating flow over topography. *Proc. R. Soc. Lond. A* **460**, 2865–2881.
- ZEITLIN, V., MEDVEDEV, S. & PLOUGONVEN, R. 2003 Frontal geostrophic adjustment, slow manifold and nonlinear wave phenomena in one-dimensional rotating shallow water. Part I. Theory. *J. Fluid Mech.* **481**, 269–290.

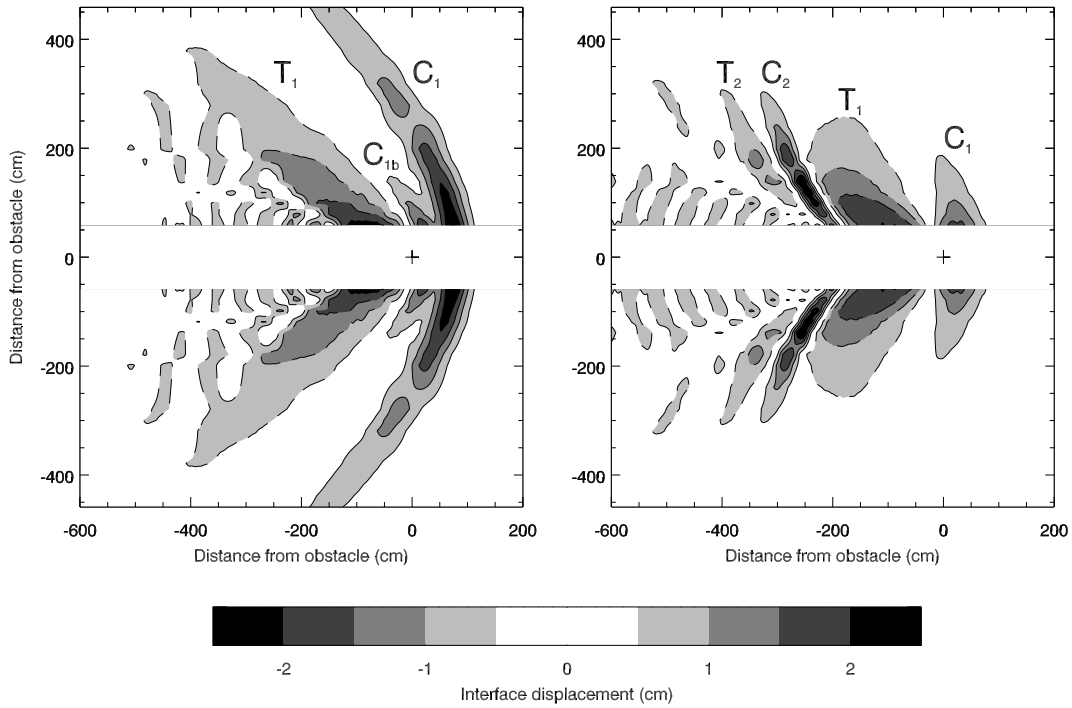


FIGURE 1. Observed experimental interface elevations for an oblong obstacle towed at speed $U = 10 \text{ cm s}^{-1}$ through the shallow layer of a two-layer fluid ($H_1 = 6 \text{ cm}$, $H_2 = 54 \text{ cm}$). Left panel: Non-rotating experiment. Right panel: Rotating experiment. The Froude number for both experiments (ratio of towing speed to interfacial gravity wave speed) is estimated to be in the range $F = 1.1 - 1.3$, and the nondimensional mountain height is $M = 0.5$. For the rotating experiment the period is $T = 120 \text{ s}$, corresponding to an inverse Burger number $B \approx 0.5$. In each panel the centre of the obstacle is marked by the '+' at the origin. Solid contours show regions where the interface rises (crests, marked C) and dashed contours depressed regions (troughs, marked T). Adapted from Johnson *et al.* (2006, see their Fig. 5).

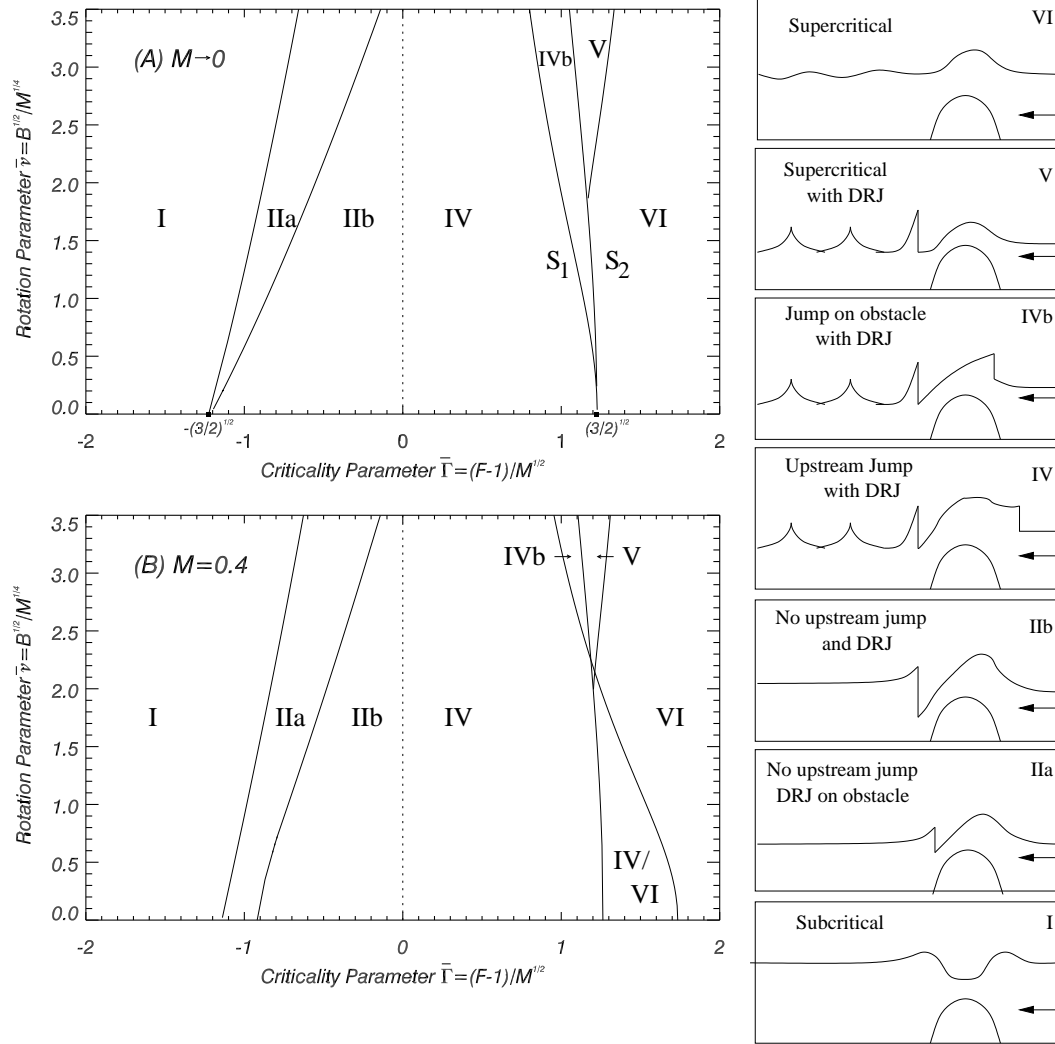


FIGURE 2. The different flow regimes for steady rotating flow over a two-dimensional parabolic ridge derived from Esler *et al.* (2005). Results depend on the three parameters, M (non-dimensional obstacle height), F (Froude number of upstream flow) and B (inverse Burger number), and are presented here as a function of the similarity parameters $\bar{\Gamma} = (F - 1)M^{-1/2}$ and $\bar{\nu} = B^{1/2}M^{-1/4}$. In the weakly nonlinear limit $M \rightarrow 0$ (upper panel) the positions of the boundaries between different flow regimes in $(\bar{\Gamma}, \bar{\nu})$ parameter space become independent of M . The lower panel shows the position of the regime boundaries at finite $M = 0.4$. A number of flows show downstream recovery jumps (DRJ).

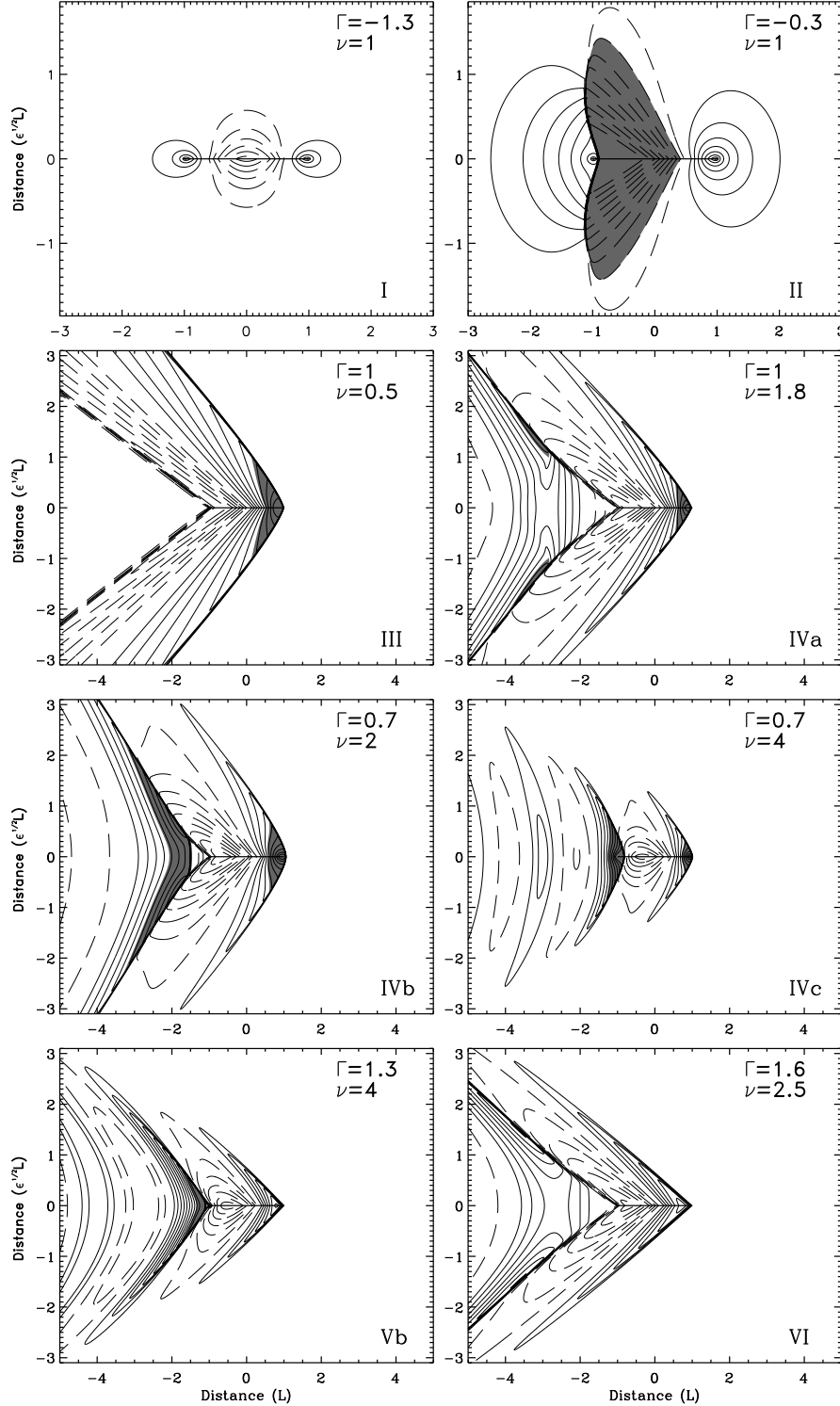


FIGURE 3. Steady state height fields illustrating various regimes in the rTSD equation (2.18) discussed in the text. Results are for the paraboloid obstacle, and are derived from numerical solutions of the rTSD equation, with spatial resolution $\delta x = \delta y = 0.01L$. Contour intervals are $0.1\epsilon H$ in each panel ($\epsilon = M^{2/3}$). Values of Γ , ν are given in the top right of each panel; Roman numerals in the bottom right corner of each panel indicate to which region of the regime diagram (Figure 1) each solution belongs, the exact location of each solution being indicated in Figure 4 by a triangle. Regions of subcritical flow are shaded, except for the top right panel where the shaded region indicates supercritical flow.

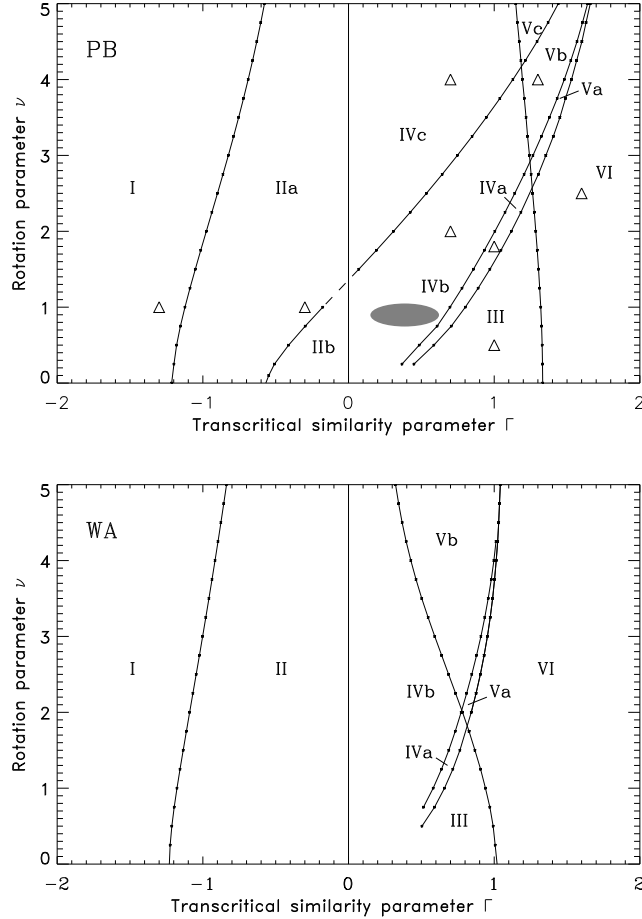


FIGURE 4. Transcritical similarity parameter and rotation similarity parameter (Γ, ν) regime diagrams for steady solutions to the rTSD equation (2.18) corresponding to flow over the paraboloid (upper panel) and ‘Witch of Agnesi’ (lower panel) obstacles. Triangles denote the location of the example flows in Fig. 4. The grey ellipse gives the approximate position of the experiment described in connection with Fig. 1. The regimes for the paraboloid are as follows: (I) Subcritical flow everywhere. (IIa) Subcritical oncoming flow with a single embedded region of supercritical flow extending behind the obstacle. (IIb) Subcritical oncoming flow with a single embedded region of supercritical flow on the obstacle. (III) Supercritical oncoming flow with a single embedded region of subcritical flow enclosing the leading edge of the obstacle. (IVa) Supercritical oncoming flow with three embedded regions of subcritical flow. (IVb) Supercritical oncoming flow with two regions of subcritical flow; the rear of which lies behind the trailing edge of the obstacle. (IVc) Supercritical oncoming flow with two regions of subcritical flow; the rear of the trailing edge of the obstacle. (Va) Supercritical oncoming flow with two embedded regions of subcritical flow both behind the trailing edge of the obstacle. (Vb) Supercritical oncoming flow with a single region of subcritical flow behind the trailing edge of the obstacle. (Vc) Supercritical oncoming flow with a single region of subcritical flow enclosing the trailing edge of the obstacle. (VI) Supercritical flow everywhere. Regimes for the ‘Witch of Agnesi’ obstacle (lower panel) are as for the paraboloid, except that the distinction between ‘on’ and ‘off’ the obstacle can no longer be made since the ‘Witch of Agnesi’ obstacle is not compact.

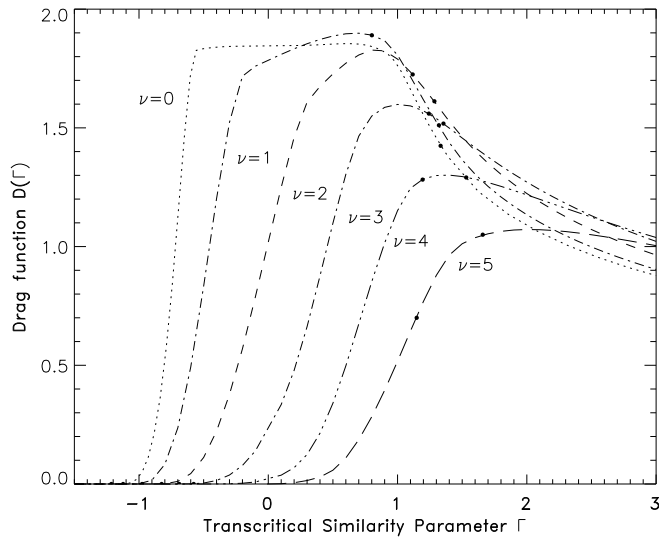


FIGURE 5. The drag function $D(\Gamma, \nu)$ as a function of the transcritical similarity parameter Γ for various fixed values of the rotation similarity parameter ν , calculated from a series of steady numerical solutions of the rTSD (2.18) equation for the paraboloid (PB) obstacle forcing given by (2.21). The dots on each curve give the value of Γ at the supercritical limit of the transcritical regime. For larger values of Γ the drag is well-approximated by linear theory.

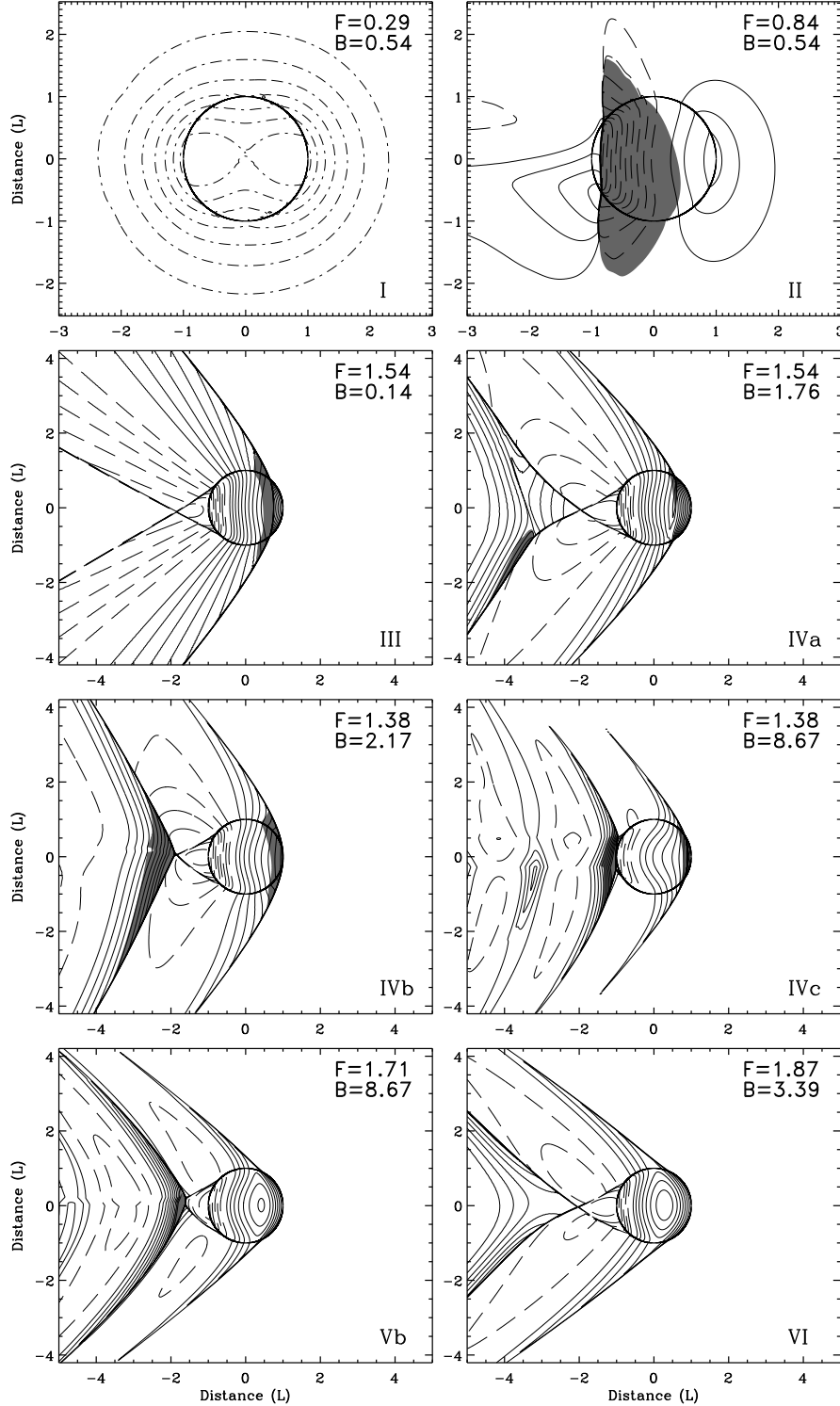


FIGURE 6. Steady state height fields for rotating shallow water flow over the paraboloid obstacle with non-dimensional height $M = 0.4$. Results are derived from numerical solutions of the rotating shallow water equations, with spatial resolution $\delta x = \delta y = 0.01L$. Contour intervals are $0.1\epsilon H$ in each panel, except for the top left panel in which the contour interval is $0.01\epsilon H$. Values of F , B are given in the top right of each panel and correspond to the values of Γ, ν in Figure 3. Roman numerals in the bottom right corner of each panel indicate the region of the regime diagram (Figure 4) to which each solution belongs, the exact location of each solution being indicated in Figure 4 by a triangle. Regions of subcritical flow are shaded, except for the top right panel where the shaded region indicates supercritical flow.

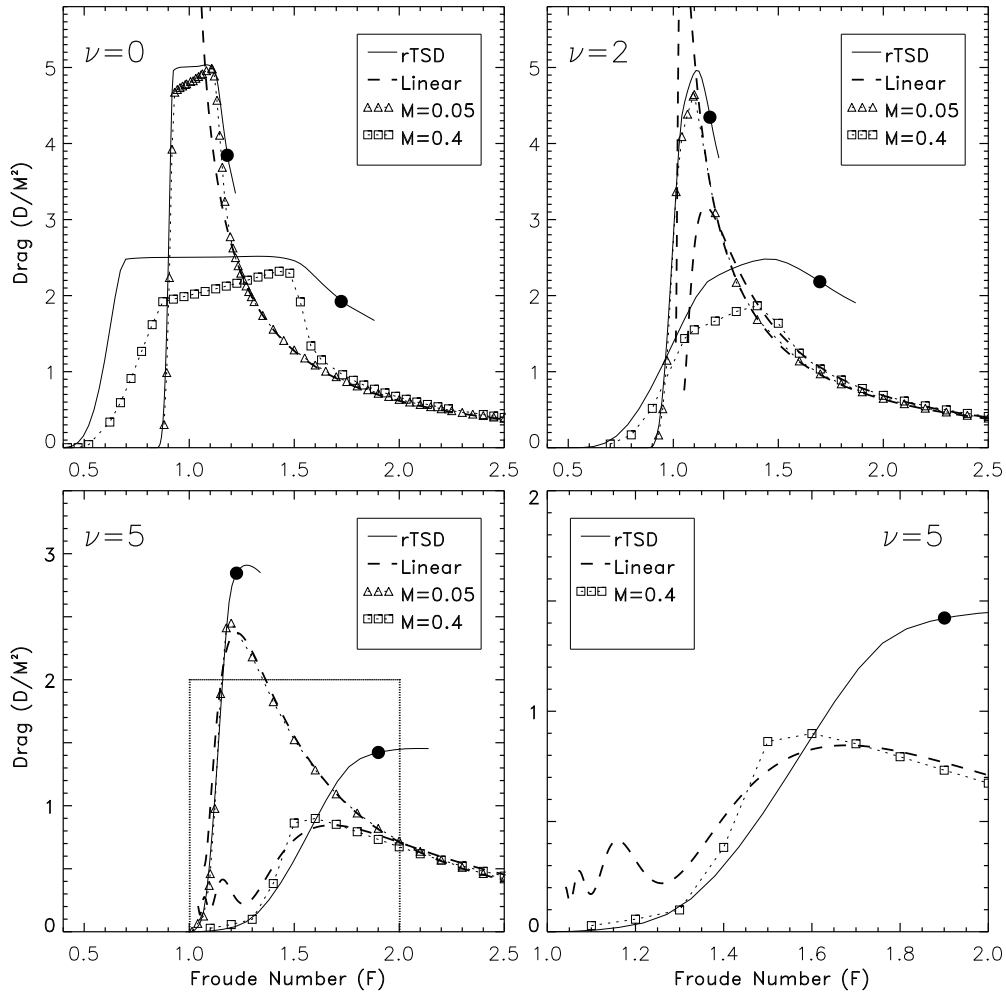


FIGURE 7. Drag D , scaled by obstacle height M^2 , as a function of Froude number F for flow over the paraboloid obstacle with the rotation parameter $\nu = 0, 2, 5$. Triangles and squares each mark the results of rotating shallow water model results for $M = 0.05$ and 0.4 respectively. The solid lines show the transcritical similarity theory predictions for the drag in each case, as derived from the rTSD numerical results (see also Fig. 5), with the Froude number corresponding to the supercritical transition marked as a solid circle. The dashed curve shows the drag calculated for linear supercritical flow.

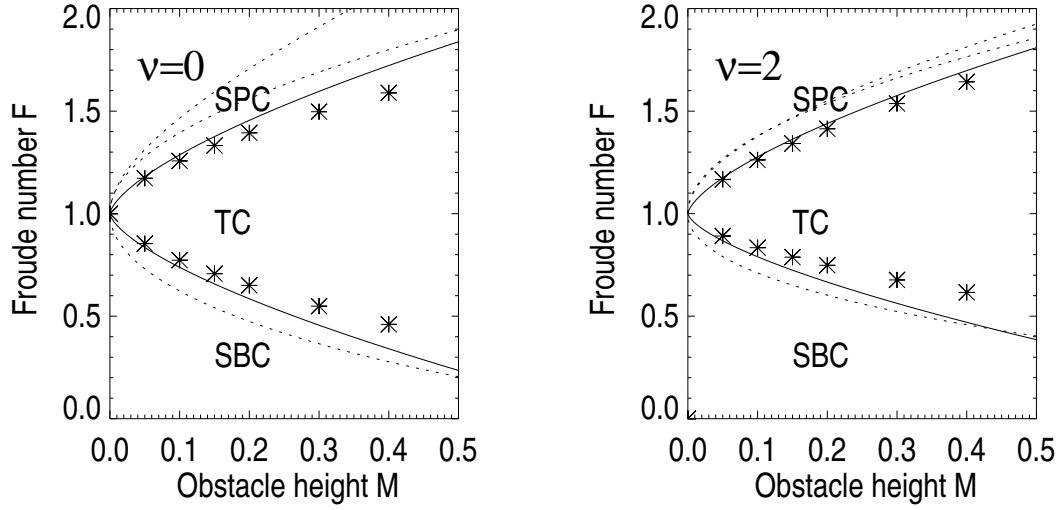


FIGURE 8. The flow regimes (SBC - subcritical, TC - transcritical, SPC - supercritical), in obstacle height - Froude number (M, F) parameter space, for flow over the paraboloid obstacle with $\nu = 0$ (non-rotating) and $\nu = 2$ (rotating). The solid lines show the predictions for the supercritical and subcritical transitions calculated from the rTSD solutions ($F = 1 + \Gamma_+ M^{2/3}$, $F = 1 - \Gamma_- M^{2/3}$, for numerically determined constants Γ_+ , Γ_-). The dotted curves show the corresponding results for a two-dimensional obstacle, valid for all M . The non-rotating 2D obstacle curves are valid for any obstacle shape and are given by, e.g. Baines (1995). The rotating 2D obstacle curves are particular to a parabolic obstacle, and are discussed in Esler *et al.* (2005). Note that there are two curves on the supercritical side, as in the 2D obstacle case a region of hysteresis exists in both non-rotating and rotating flow (e.g. Baines 1995). The stars show the location of the actual transitions found in each case from a sequence of steady numerical solutions of the rotating shallow water equations (2.1).

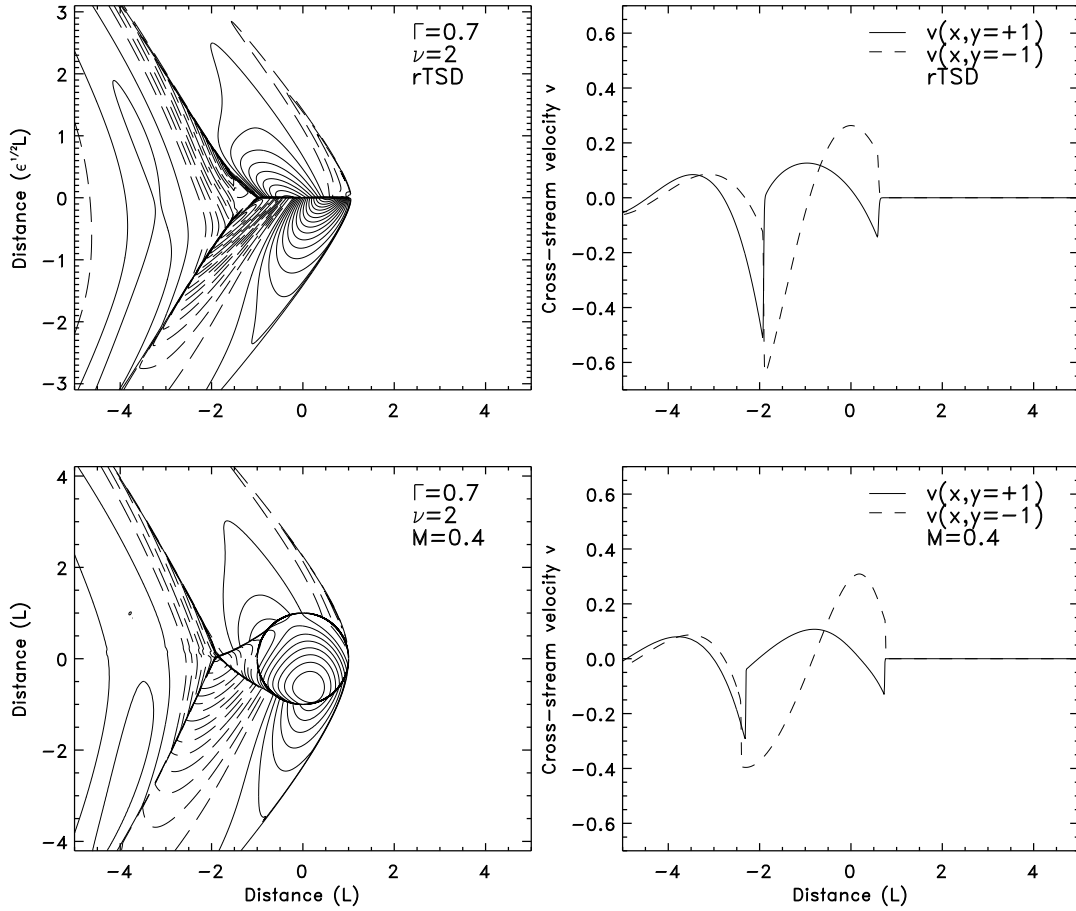


FIGURE 9. Upper panels: (Left) Contour plot of the leading order transverse velocity field $v_0^o(x, Y)$ diagnosed from the rTSD solution for flow over the paraboloid (PB) obstacle with $\Gamma = 0.7$ and $\nu = 2$. The contour interval is $0.1\epsilon^{3/2}c$, (note that $\epsilon^{3/2} = M = 0.4$ allows comparison with the lower panel results). (Right) Cross-sections of $v_0^o(x, Y)$ at $Y = 0.4^{1/3} = 0.7368$ (solid curve) and $Y = -0.7368$ (dashed curve). (These values of Y are chosen to correspond to the edge of an obstacle of unit radius when $M = 0.4$ as below, and the v -axis is also scaled by $\epsilon^{3/2} = M = 0.4$). Lower panels: (Left) As for the upper panels but for $v(x, y)$, the solution of the rotating shallow water equations for the PB obstacle with $M = 0.4$, $F = 1.3800$, $B = 2.1715$ (giving $\Gamma = 0.7$ and $\nu = 2$), with contour interval $0.04c$. (Right): Cross sections of $v(x, y)$ at $y = 1$ (solid curve) and $y = -1$ (dashed curve).